

Photon echoes and two dimensional spectra of the amide I band of proteins measured by femtosecond IR – Raman spectroscopy

Paul. M. Donaldson

Central Laser Facility, RCaH, STFC Rutherford Appleton Laboratory, Harwell Science and Innovation Campus, Didcot, OX11 0QX, UK

Supplementary information

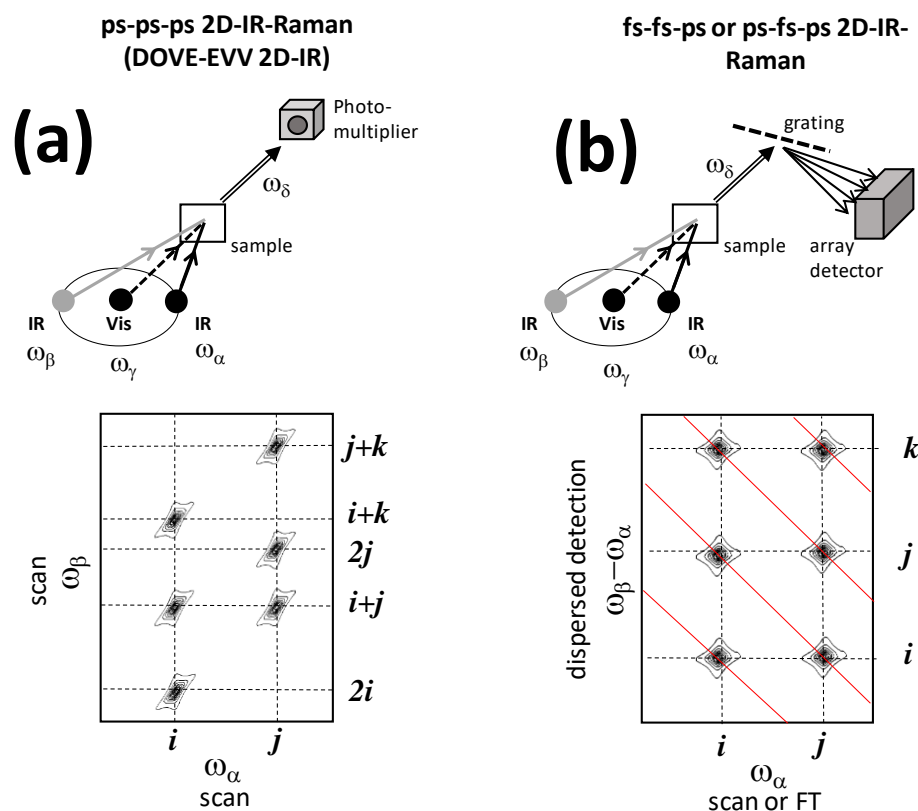


Figure S1. A comparison of the ps-ps-ps DOVE-EVV 2D-IR-Raman approach and the fs-fs-ps and ps-fs-ps 2D-IR-Raman approaches discussed in the main text. i , j and k are different vibrational states. $i+j$ and $2i$ are combination bands and overtones respectively.

Section 1. IR-Raman spectra

In this section, the consequences of replacing one or both of the narrowband ps infrared beams of the ps-ps-ps DOVE-EVV 2D-IR-Raman approach with broadband fs beams are discussed in the context of how the 2D spectra appear along the detection axis.

Figure 2a in the main text shows the ‘all-picosecond’ (ps-

ps-ps) scheme of Wright.¹ Figures 2b-2d show the replacement of one or both of the ps IR pulses α and β with broadband fs IR pulses. For every experiment conducted in the main text, the β pulse was femtosecond and therefore broadband. With this replacement, the emitted IR-Raman signal is no longer narrowband and not advantageously detected on a single detector (as in Figure S1a for DOVE-EVV) but better dispersed onto an array detector for analysis in a manner similar to broadband SVFG (Figure S1b).

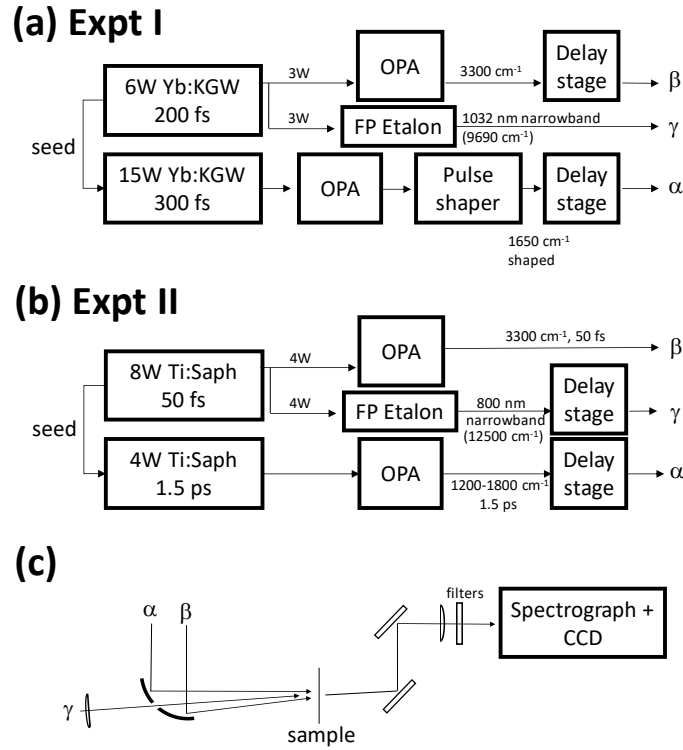


Figure S2. Schematics of IR-Raman experiments described in the main text. (a) The Yb-based femtosecond laser system with mid-IR pulse-shaping (LIFETIME laboratory) (b) The Ti:Sapphire-based dual femtosecond-picosecond laser system delivering a ‘bright α pulse’ (c) The geometry of the beam focusing and spectrometer in both experiments (Ultra A laboratory).

A practical consequence of measuring the IR-Raman signal’s ω_s frequency distribution rather than its integrated intensity is that after subtracting the constant visible γ frequency, the dispersed detection axis gives a measure of the difference frequency $\omega_\beta - \omega_\alpha$. This amounts to a 45 degree rotation in the 2D-IR-Raman spectrum compared with DOVE-2D plots in the literature, as shown in Figure S1. Lines of constant ω_β are shown in red in the Figure S1b dispersed detection scheme. In the 2D measurements, where the signal response to ω_α is resolved, rather than measuring the combination band / overtone frequency, as is the case in S1a, we observe the frequency of the states of the combination band *after* subtraction of the ω_α driven fundamental frequency involved. The observed emission frequency may potentially be anharmonically shifted (depending on the source of the anharmonicity giving rise to the overtone or combination band). Similar to DOVE-EVV 2D-IR spectra, pathway 3 processes appear anharmonically shifted along ω_α also. Finally, as is shown in Section S3, $\omega_\beta - \omega_\alpha$ is actually the frequency at which the nonlinear polarization oscillates during the second coherence time period, so IR-Raman and 2D-IR frequency axes correspond as $\omega_\alpha \Leftrightarrow \omega_1$ (or ω_{pump}) and $\omega_\beta - \omega_\alpha \Leftrightarrow \omega_3$ (or ω_{probe}).

For the IR-Raman dispersed echo approach outlined in the main text, there is no ω_α frequency resolution. The conse-

quence of this can be understood in Figure S1b by projection of the ω_α frequency axis onto the $\omega_\beta - \omega_\alpha$ frequency axis. Overtones and combination bands involving a common state then overlap along the $\omega_\beta - \omega_\alpha$ axis of the dispersed IR-Raman Photon echo data.

Section 2. Lasers and spectrometers

The experiments conducted on two laser systems at the Central Laser Facility (STFC Rutherford Appleton Laboratory) will be denoted Experiment I – the pulse shaped femtosecond spectrometer (LIFETIME laboratory) and Experiment II – the ‘bright α pulse’ spectrometer (Ultra A laboratory). They are displayed schematically in Figure S2. The key conceptual difference between Experiments I and II is that in Experiment I the mid-IR α pulse is pulse shaped from a 300 fs optical parametric amplifier (OPA) source and in Experiment II it is generated from a bright, tuneable picosecond OPA. It is emphasised here that the pairs of synchronised dual regenerative amplifiers used are actually not necessary for IR-Raman spectroscopy - they are part of the Central Laser Facility’s approach to the delivery of a range of spectroscopic techniques.^{2,3} A single femtosecond regenerative amplifier system could be used in Experiments I and II, the output of which would be split appropriately to drive 2 independently tunable OPAs for generating the α and β pulses and into a third beam to pass

through Fabry-Perot etalons or bandpass filters for generating the γ pulse. For experiment II, the bright picosecond pulse can be generated from an OPA using second harmonic bandwidth compression,⁴ a technique now commercially available.

Experiment I. Laser detail

Experiment I (Figure S2a) is based on a 100 kHz Yb:KGW dual-Pharos laser system (Light Conversion) described in detail previously.^{2,3} This system comprises two Yb:KGW amplifiers seeded from the same oscillator. The 6W 1032 nm output of the shorter pulse amplifier (Light Conversion Pharos SP) was split into two. Half was used to pump a KTA-based OPA (Orpheus-1, Light Conversion) generating tuneable broadband infrared (3300 cm^{-1} for the present experiments) and the other half filtered to 12.5 cm^{-1} bandwidth using a Fabry-Perot etalon (Tecoptics). These formed the β and γ pulses of the IR-Raman experiment. As the setup was normally used as a facility for 2D-IR and TR-IR spectroscopy, the 1032 nm γ beam was sourced from a pump beam originally routed through an additional OPA. For convenience (easier temporal synchronisation to the α and β beams) the beam-path through the OPA was retained, but all OPA crystals and dichroic mirrors were removed from the OPA to allow the γ beam to pass through.

The longer-pulse regenerative amplifier (Light Conversion 15W Pharos HP) pumped a single OPA (Orpheus-HP, Light Conversion) generating mid-IR light in several stages (BBO->KTA->GaSe). The output of this OPA was sent through a mid-IR pulse shaper based on a Germanium acousto-optic modulator placed in a 4F arrangement⁵ (Phasetech Quickshape). The pulse shaper was aligned, calibrated and GVD compensated at $\sim 1640\text{-}1650$ cm^{-1} centre wavelength. The output of the pulse shaper formed the α beam.

Experiment I. 2D-IR-Raman spectrometer

The α , β and γ pulse trains output from the OPAs were collimated with lenses (γ , β) and a curved mirror (α) to several mm diameter FWHM. IR-Raman signal generation used the focussing scheme in Figure S2c. The α and β pulses were focussed using 75 mm focal length 90 degree off-axis gold parabolic mirrors and the γ pulses were focussed using a 300 mm focal length plano-convex lens. A hole in the centre of the parabolic mirror permitted the γ gamma pulse to pass through, with all three beams in the same plane (Figure S2c). The angles between the beams were minimal ($<10^\circ$). As the samples were thin, phase matching issues were not a concern. The polarisation of the beams was PPP. A customised microboulometer array⁶ was used to optimise the size and overlap of the α and β beams. A beam profiling camera (Thorlabs) was used to find the size of the γ beam at the sample focus. Adjustments to the γ size at the sample focus were made by defocussing the γ lens to make the γ size $\sim 50\%$ bigger than the α and β sizes. The

α and β focussed spots were measured as ~ 50 μm FWHM. All optics were enclosed and purged in N_2 .

On initial setup, temporal overlap of the beams was found by using the existing capabilities of the LIFETIME laboratory for measuring 2D-IR spectra. The α pulse was chopped and its Kerr effect in Ge or ZnSe detected using either the 1032 nm γ or the 3300 cm^{-1} β pulses as probe beams, each illuminating the MCT arrays normally used for 2D-IR spectroscopy. With the beams temporally and spatially overlapped, as well as the detected Kerr effect, the emission of visible beams could be observed by eye from ZnSe (bright), ZnS (bright) or CaF_2 (weaker) in each case corresponding to various nonlinear mixing processes involving pairs of the α , β or γ pulses. Care had to be exercised to compensate for slight timing shifts due to dispersion when exchanging these materials – these were large enough to extinguish the nonlinear signals of interest.

The IR-Raman light emerging from the sample was collimated with a +150 mm plano convex lens, filtered to remove the γ beam using a pair of OD6 Semrock edgepass filters and routed to a purpose-built spectrograph comprising a grating (600 lines / mm, Thorlabs) mounted on a motorised rotation stage and a +200 cm curved mirror focusing the light onto a CCD camera (Andor IduS BEX2.DD). A spectral resolution of $\sim 5\text{-}6$ cm^{-1} was achieved for a detector limit of 2 cm^{-1} per pixel

After finding temporal and spatial overlap of the α , β or γ pairs of beams (as described above), a CaF_2 window was positioned at the 3-beam focus. The experiment was built and aligned from scratch on four occasions, and each time it was always the case that the positioning of the window in the focus and the timing of the three beams were not optimal for IR-Raman signal generation. This would make finding the correct alignment of the optics for routing the IR-Raman signal from the sample to the spectrometer the most challenging aspect of configuring the experiment. On finally observing and optimising the $\omega_\gamma + \omega_\beta - \omega_\alpha$ nonresonant background on the CCD camera, a blueish nonlinear emission involving all three beams α , β and γ could be observed by eye. This was not the $\omega_\gamma + \omega_\beta - \omega_\alpha$ emission (880 nm) or $\omega_\gamma + \omega_\beta + \omega_\alpha$ (683 nm) but some other higher order process occurring in the CaF_2 .

The mid-IR pulse-shaper for the α beam was calibrated using atmospheric water lines. Calibration of the detection axis $\omega_\gamma + \omega_\beta - \omega_\alpha$ was achieved using the emission lines of an Hg-Ar lamp. The second harmonic of the 1032 nm γ pulse was measured on a calibrated spectrograph (Thorlabs) to determine the exact wavenumber value of the γ pulse and therefore obtain $\omega_\beta - \omega_\alpha$. Despite repeated attempts, the most accurate calibrations of the $\omega_\beta - \omega_\alpha$ axis were not reproducible to better than ± 20 cm^{-1} . This was due to the homemade spectrometer used lacking an entrance slit and the inaccurate positioning/coupling of the

HgAr lamp beam into the experiment. The $\omega_\beta - \omega_\alpha$ axis derived from the CCD camera of Experiment I data was corrected using the position of the alpha-helical protein BSA overtone signal established in Experiment II, which used a commercial spectrograph with an entrance slit. The peak was observed to be $\sim 15 \text{ cm}^{-1}$ anharmonically shifted along $\omega_\beta - \omega_\alpha$ compared with the peak along ω_α ($\sim 1650 \text{ cm}^{-1}$).

The maximum pulse energies incident on the sample for α , β and γ were 0.3, 1 and 2 μJ @100 kHz. At these levels, the air-exposed protein film samples studied were observed to slowly degrade. The degradation timescales appeared to respond linearly to laser power, indicating that the degradation was thermal. Cracked films tended to be less-well adhered to the substrate, resulting in faster degradation. The α , β and γ pulse energies used for data collection were 0.3, 0.2 and 0.7 μJ , with the repetition rate reduced to 50 kHz, corresponding to a 30x reduction in power compared with the maximum. As the damage was thermal, it would have been advantageous in terms of signal-to-noise to maintain the highest pulse energies and drop the repetition rate of the laser, however the pulse-shaper was configured for 50-100 kHz operation and reconfiguring/recalibration of this part of the experiment was beyond the time available.

The collection of data was automated using Labview to control inter-pulse delays, to read out the CCD camera and to update pulse-shaper masks for frequency or time domain scans. The calibrated and GVD compensated pulse shaper was configured to output either a reverse etalon shaped pulse of defined centre frequency and 5-20 cm^{-1} width,⁷ or a pair of Gaussian pulses with fixed delay. The acquisitions proceeded in a step-scan manner, updating the pulse shape to change the pulse centre frequency or timing, then signal averaging on the CCD camera for 0.2 - 2s and repeating. Frequency domain datasets could be plotted without further processing. Time domain heterodyne signal interferograms were symmetrised, windowed (Hanning), zero padded and fast Fourier transformed, taking the real part of the signal. Examples of an interferogram from a protein are shown in Figure 10a - 10c of the main text. The resulting Fourier transformed data is shown in 10d. Shown in 10e is a spectrum of the nonresonant background. Once in the form of 10d and 10e, Equation 16 (see ESI Section 4) was applied to calculate the heterodyne spectrum.

Experiment II. Laser detail

Experiment II is based on a 10 kHz dual ps - fs Ti:Sapphire laser system⁸ (Thales) comprising separate modules of stretcher, regenerative amplifier, cryogenically cooled multipass amplifier and compressor fed by a common seed train. Similar to Expt I, the short-pulse 50 fs 800 nm amplifier output was split. 4W was used to pump a two-stage BBO OPA with difference frequency generation in AgGaS₂

(Light Conversion, Topas). This generated tuneable femto-second mid-IR light (here set to 3300 cm^{-1} to form the β pulse). The remaining 4W of femtosecond 800 nm light was reduced to 2W with a beamsplitter and for timing purposes passed through an OPA 'chassis' with its crystals and dichroic mirrors removed, and then passed through a 12.5 cm^{-1} width Fabry-Perot etalon (Tecoptics) to form the γ pulse. For the α pulse, 4W of the 800 nm ps amplifier output pumped a tuneable multipass BBO OPA seeded by super-fluorescence and generating mid-IR by difference frequency generation of the signal and idler in AgGaS₂ (Light Conversion, ps-Topas). All optics were enclosed and purged in N₂.

Experiment II. Spectrometer

The α , β and γ pulse trains output from the OPAs were collimated with lenses (γ) or curved mirrors (α , β) giving roughly 3-4 mm FWHM collimated beams. The focussing scheme in Figure S2c was used for IR-Raman signal generation. The α and β pulses were focussed using 7.5 cm focal length 90 degree off-axis gold parabolic mirrors and the γ pulses were focussed using a 500 mm focal length plano-convex lens. A hole in the centre of the parabolic mirror permitted the γ gamma pulse to pass through, with all three beams in the same plane (Figure S2c). The angles between the beams were minimal ($<10^\circ$). As the samples were thin, phase matching issues were not a concern. The polarisation used in experiments was PPP. A microboulometer array⁶ was used to find the size and overlap of the α and β beams. A beam profiling camera (Thorlabs) was used to find the size of the γ beam at the sample focus. Adjustments to the γ size at the sample focus were made by defocussing the γ lens to make the γ size $\sim 50\%$ bigger than the α and β sizes. The α and β focussed spots were measured to be 30-40 μm FWHM. The maximum pulse energies incident on the sample were 0.2-0.5, 1.5 and 3 μJ at 10 kHz. Although thermal damage was not thought to be an issue, the tighter focussing and higher peak intensities of the β and γ pulses compared with Experiment I (as well as the shorter wavelength of the γ pulses) caused slow (~ 20 minutes) protein signal degradation. Consequently the pulse energies of these two beams were reduced for studying the protein films. Energies of 0.2-0.5, 0.4 and 0.4 μJ /pulse for α , β and γ respectively were used at 10 kHz.

The light emerging from the sample was collimated with a +150 mm plano convex lens and filtered to remove the γ beam using a pair of OD6 Semrock edgepass filters. A commercial spectrograph (Holospec equipped with an HSG-632.8-LF grating) was used, the advantage compared with Experiment I being the addition of an entrance slit to reject stray light and provide a fixed spectrum calibration and easier adjustment of the focussing on the CCD camera (Andor Idus BEX2.DD). A spectral resolution of $\sim 5-6 \text{ cm}^{-1}$ was achieved for a theoretical maximum of 2 cm^{-1} / pixel.

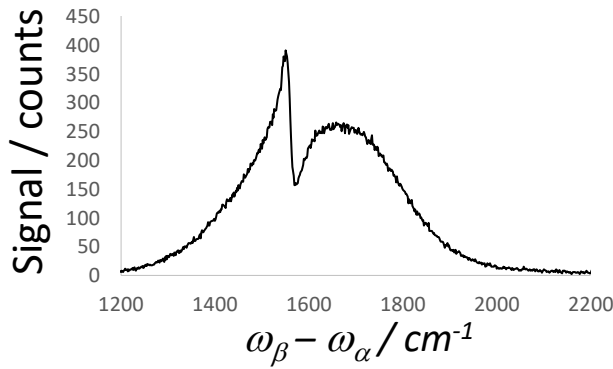


Figure S3 A nonlinear signal generated in air (no sample) involving the three IR-Raman beams and emitting at the same wavelengths as the Amide I. Observed in Experiment 2 only.

The procedure for finding temporal overlap of the pulses and location of the IR-Raman $\omega_\gamma + \omega_\beta - \omega_\alpha$ nonresonant background signal of CaF₂ was similar to that described for Experiment 1. Again, proper alignment of the setup resulted in the emission of visible light from the CaF₂ window involving all three beams. With the beams properly overlapped, a nonlinear signal from just the N₂ purge gas (no sample) was observed on the CCD camera (Figure S3). The origins of this signal were not fully understood. With incorrect positioning of the sample in the laser focus, this signal could potentially interfere with the sample signal.

Calibration of the detection axis $\omega_\gamma + \omega_\beta - \omega_\alpha$ across the spectrometer CCD array was achieved using an HgAr lamp. The wavelength of the 800 nm γ pulse was measured accurately using a calibrated fibre-coupled spectrometer (Thorlabs). This measurement of ω_γ was then used to obtain $\omega_\beta - \omega_\alpha$. The α pulse frequencies were calibrated using atmospheric water lines.

The collection of data was automated using Labview to read out the CCD camera, to step inter-pulse delays and to step the frequency of the ps OPA. It was observed that the time of the arrival of the α pulse at the sample varied as a function of frequency over 1200-1800 cm⁻¹. This was largely due to dispersion from optical components within the beam path. For example, a 2 mm CaF₂ window in the beam caused a 1.5 ps timing change across a scan. A correction for each α frequency value was pre-measured through nonresonant background cross correlations and then applied during data acquisition.

The effect of atmospheric water vapour absorption in the α - beam optics,

At long $T_{\alpha\gamma}$ delay times, additional complex structures were observed in pathway 1 homodyne 2D-IR-Raman spectra when using frequency narrowed pulses. Combined with the elongation of improperly rephased, inhomogeneously broadened spectra and the multiple beatings observed in

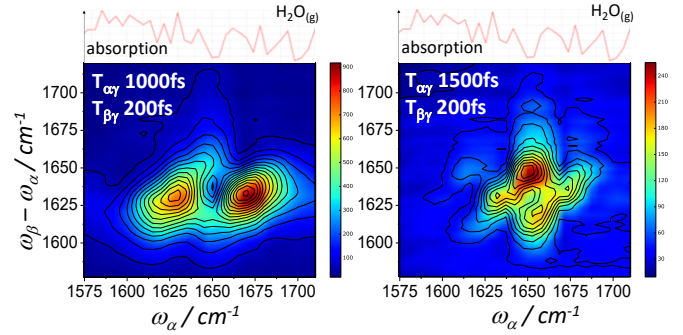


Figure S4 An illustration of how atmospheric water absorption in the α beam optics can cause artefacts in homodyne frequency domain 2D-IR-Raman spectra (BSA).

systems with complex bandshapes such as ConA, confusion could easily arise trying to interpret so many strange spectral features. The latter effects are mitigated through the use of heterodyne detection, or $T_{\alpha\gamma} \leq 2T_{\beta\gamma}$ delays. Any additional structures in the spectra were caused by the presence of water vapour in the α -beam optics. This effect is not simply an 'imprint' of the water absorption on the ω_α spectral axis, as is the case at earlier $T_{\alpha\gamma}$ delays, or for heterodyne FT-2D-IR-Raman (or 2D-IR spectroscopy). The narrow water absorption lines cause the narrowed α -pulse to ring at later times. These 'satellite' fields generate unwanted IR-Raman signal in patterns of increasing complexity as a function of delay. An example is shown in Figure S4 for BSA – which should have a continuous distribution of intensity across the ω_α axis, but under poor purging is distorted at the frequency of the strongest water absorption feature.

Section 3. IR-Raman response functions and signal simulations

In this section, the formal link between 2D-IR-Raman and 2D-IR spectroscopy is made. The notation and construction of response functions are described clearly by Hamm and Zanni.⁹ For 2D-IR spectroscopy, there are six response functions required to describe the signals from a three level anharmonic oscillator – three of which are rephasing and three nonrephasing. In Figure S5, the so-called 'third' 2D-IR response function 'R₃' is compared with that of IR-Raman pathway 1. Both are expressed in the 'slow modulation' (inhomogeneous limit). In the IR-Raman response function, there are three conventions to note:

- 1) $\gamma_{21} = \gamma_{20} + \gamma_{10}$ and $\omega_{21} = \omega_{20} - \omega_{10}$
- 2) For simplicity '1-2' gap dephasing¹⁰ is neglected.
- 3) The third coherence time period t_3 in the IR-Raman diagram is nonresonant and therefore the nonlinear polarization has no response outside of the γ pulse envelope. Although resonant studies are interesting, the nonresonant Raman response serves no purpose in discussions here and

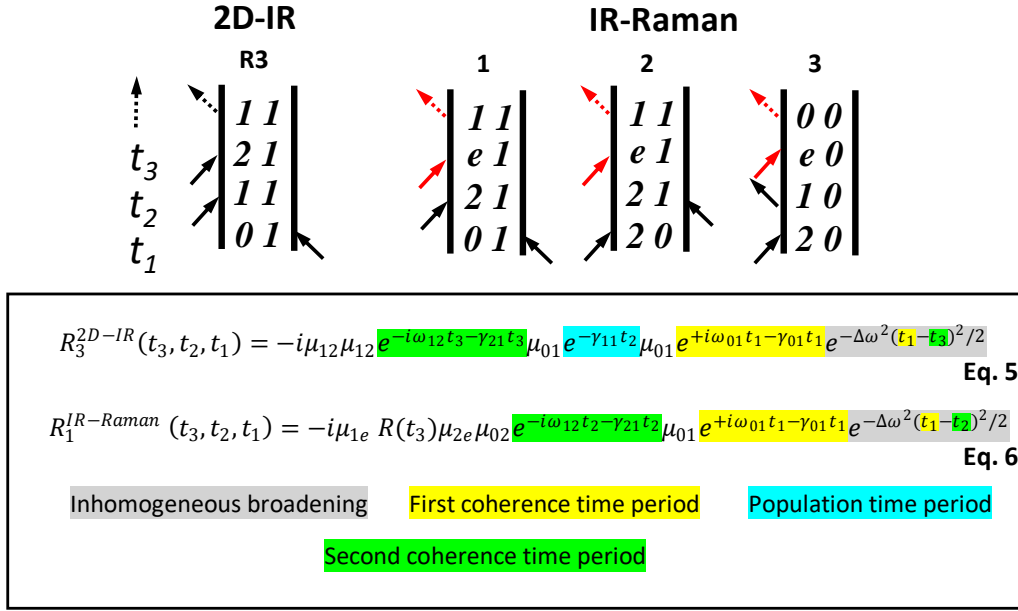


Figure S5 2D-IR and IR-Raman Feynman diagrams for a three-level anharmonic oscillator (quantum states 0, 1 and 2) and an off resonant electronic state e . The ‘anti-resonant’ diagrams for the IR-Raman processes (third field arrows pointing outward) are not shown. Far from electronic resonance, these give identical signals to the resonant terms. Shown in the box are the response function equations of 2D-IR R_3 and IR-Raman diagram 1. The time periods and inhomogeneous broadening are color-shaded for clarity.

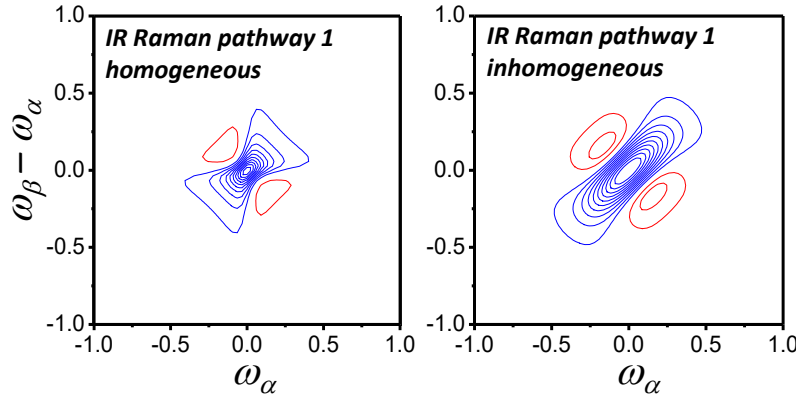


Figure S6. Calculations of the 2D-IR-Raman signal field’s spectrum for rephasing diagram 1 in the impulsive limit for homogeneous broadening (left) and inhomogeneous broadening (right). The calculations were carried out with $\omega_{01} = \omega_{12} = 0$ (rotating wave approximation). Blue depicts a negative amplitude and red positive. The open-source Mathematica code for calculating impulsive responses with a Kubo lineshape function supplied at <http://www.2d-ir-spectroscopy.com> was adapted to produce this figure.

there is no additional spectral information to be gained through it along t_3 . To make the IR-Raman response function visually easier to interpret, in Figure S5 the complex exponential term $e^{+i(-\omega_e - \omega_{12})t_3 - (\gamma_e - \gamma_{10})t_3}$ has been replaced by the term ‘ $R(t_3)$ ’.

The important point in identifying the nature of the heterodyne detected FT-2D-IR-Raman spectra in the main text is that the 2D-IR ‘ R_3 ’ response function (Eq. 5) and IR-Raman diagram 1 response function (Eq. 6) are identical along t_1 , and the IR-Raman diagram’s t_2 response is identical to the 2D-IR ‘ R_3 ’ t_3 response. Thus the IR-Raman and 2D-IR frequency axes correspond as $\omega_\alpha \Leftrightarrow \omega_l$ (or ω_{pump}) and $\omega_\beta - \omega_\alpha \Leftrightarrow \omega_3$ (or ω_{probe}).

In the impulsive limit of ‘delta function’ excitation,^{9,10} the response function describes the temporal response of the signal field. In this limit, the 2D-IR spectrum of R_3 is obtained by its Fourier Transform along t_1 and t_3 . The 2D spectrum of $R_1^{IR-Raman}$ is likewise achieved in the impulsive limit through Fourier Transform along t_1 and t_2 . The resulting 2D rephasing diagram spectra in the limit of inhomogeneous and homogeneous broadening are shown in Figure S6. The absence of a population period in the IR-Raman response is notable. Whereas both induced modulation (pure dephasing) of ω_{10} and ω_{20} frequencies on timescales shorter than population relaxation and dephasing can be observed in a 2D-IR spectrum through spectral diffusion as a function of t_2 , no direct equivalent measurement is possible

with IR-Raman pathway 1. Discussions on how spectral diffusion might enter the 2D-IR-Raman spectra will be left for future work.

The nonrephasing IR- Raman response functions for IR-Raman pathways 2 and 3 are:

$$R_2^{IR-Raman}(t_3, t_2, t_1) = -i\mu_{1e} R(t_3)\mu_{2e}\mu_{01} e^{-i\omega_{12}t_2 - \gamma_{21}t_2} \mu_{02} e^{-i\omega_{02}t_1 - \gamma_{20}t_1} e^{-\Delta\omega^2(t_1+t_2)^2/2} \quad \text{Eq. 7}$$

$$R_3^{IR-Raman}(t_3, t_2, t_1) = i\mu_{0e} R(t_3)\mu_{1e}\mu_{21} e^{-i(\omega_{12}-\Delta)t_2 - \gamma_{10}t_2} \mu_{02} e^{-i\omega_{02}t_1 - \gamma_{20}t_1} e^{-\Delta\omega^2(t_1+t_2)^2/2} \quad \text{Eq. 8}$$

Again, the different time evolution periods and inhomogeneous broadening are shaded for easier interpretation. Nonrephasing pathways 2 and 3 have positive times in the inhomogeneous broadening term.^{9,10} $R_3^{IR-Raman}$ differs to the other pathways through the transition strength, anharmonicity Δ and dephasing during period t_2 . There are also two special cases to note when dealing with the single-vibration (overtone) three level system (as opposed to two-vibration (combination band) cross peaks. It was pointed out in the main text that for excitonic systems, $\gamma_{20} = \gamma_{10}$. For non-excitonic systems, we would expect $R_3^{IR-Raman}$ to dephase less rapidly during t_2 than the other two pathways. Also, assuming that the transition dipole strengths scale like that for a harmonic oscillator, we have:⁹

$$\mu_{12} = \sqrt{2}\mu_{01} \quad \text{Eq. 9}$$

This would make $R_3^{IR-Raman}$ $\sqrt{2}$ higher in amplitude than the other two pathways. For the excitonically coupled amide I band explored in the main text, it would appear that the situation is not as described above - the homodyne echo and homodyne amide I 2D-IR-Raman spectra collected show a weak pathway 3 response, implying that $\mu_{12} < \mu_{01}$. In support of this fact, close examination of many 2D-IR spectra of alpha-helical proteins in the literature indicate weaker 1->2 excited state bands.²

Studying the behaviour of the predicted signals from convolutions of the response functions with the laser pulses of envelopes $A(t)$ is extremely useful. The required integrals are of the form:

$$E_\delta(t) \propto \iiint_0^\infty dt_3 dt_2 dt_1 R_1^{IR-Raman}(t_3, t_2, t_1) A_\gamma(t - t_3) A_\beta(t - t_3 - t_2 - T_{\beta\gamma}) A_\alpha(t - t_3 - t_2 - t_1 - T_{\alpha\gamma}) \quad \text{Eq. 10}$$

Owing to the nonresonant t_3 period, under the Placzek approximation,^{10,11} Equation 10 simplifies to:

$$E_\delta(t) \propto A_\gamma(t) \iint_0^\infty dt_2 dt_1 R_1^{IR-Raman}(t_2, t_1) A_\beta(t - t_2 - T_{\beta\gamma}) A_\alpha(t - t_2 - t_1 - T_{\alpha\gamma}) \quad \text{Eq. 11}$$

The pathway 2 and 3 signals are calculated by using the appropriate response function (Eq 7 or 8) and by reversing the role of laser pulse envelopes A_α and A_β .

Using equations 6, 7, 8, 10 and 11, the effect of the single-sided exponential γ pulse on the IR-Raman spectrum was computed and explored. This has been discussed in SFG studies⁹ - the conclusion being that a single-sided exponential pulse samples the Raman free-induction decay less accurately than a Gaussian pulse. In the present work this has to be set against the big advantage of nonresonant background reduction for a single sided exponential pulse. Figure S7 shows simulated laser pulse sequences of the LIFETIME and Ultra A experiments. Use of an 800 fs Gaussian γ pulse (Figure S7 'alternative (a)') would significantly increase the 3-pulse overlap (and therefore the nonresonant background). Use of shorter pulses in a hypothetical fs-fs-ps experiment (Figure S7 alternative (b)) would however permit the use of a picosecond Gaussian γ pulse for IR-Raman photon echo or heterodyne FT-2D measurements.

Figure S8 shows simulations of the responses calculated using the laser pulses of the LIFETIME system for a three level system with all states having 12 cm^{-1} homogeneous and 80 cm^{-1} inhomogeneous broadening (and 15 cm^{-1} anharmonic shift between pathway 3 and 1+2). The 12 cm^{-1} width single-sided exponential γ pulse used in the experiments manages to convert the nonlinear response of the α and β interactions fairly well.

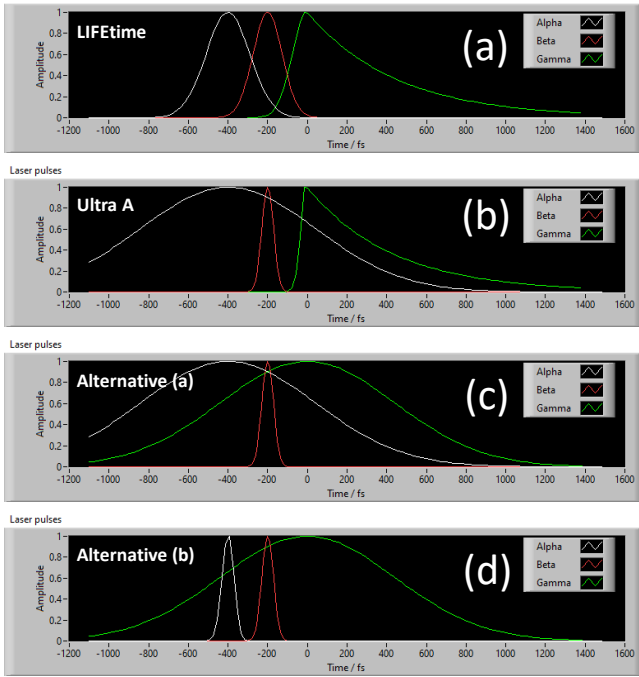


Figure S7. Laser pulse envelopes. (a) The IR-Raman dispersed echo sequence used on the LIFETIME experiment. (b) The “bright α pulse” Ultra A sequence. (c) and (d) the use of an 800 fs Gaussian γ pulse.

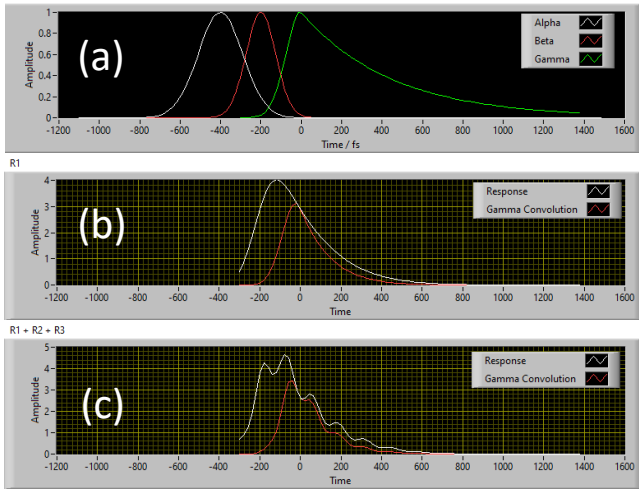


Figure S8. Simulation of the IR-Raman dispersed echo signal at a rephasing delay of $T_{\alpha\gamma} = 2T_{\beta\gamma}$. (a) The laser pulse envelopes (identical to those used in the main text). (b) The pathway 1 response integrated across t_1 and t_2 as a function of time t (white). The γ pulse ‘gates’ the response (red). (c) shows the response and gating for pathways 1, 2 and 3 combined.

The response not converted before $t=0$ is to be expected – this is the purpose of the $T_{\beta\gamma}$ delay. The mismatch between the response for $t>0$ is of concern. The conversion error broadens the observed spectrum.⁹ The conversion improves for longer interpulse delays but is ~ 2 worse for delays around temporal overlap. An 800 fs (20 cm^{-1}) Gaussian pulse does give much more accurate conversion (Figure

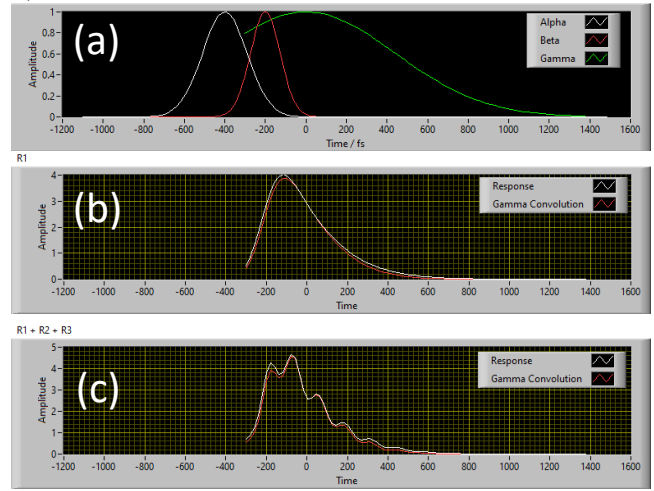


Figure S9. Simulation of the IR-Raman dispersed echo signal at a rephasing delay of $T_{\alpha\gamma} = 2T_{\beta\gamma}$ using a Gaussian shaped γ pulse. (a) are the laser pulse envelopes. In (b), the response integrated across t_1 and t_2 as a function of time t is shown for pathway 1 (white). The γ pulse ‘gates’ the response (red). (c) shows the response and gating for pathways 1, 2 and 3.

S9).

In conclusion, although the interpretation of the data in the main text remains sound for the chosen laser pulses, the optimum implementation of the γ pulse for future IR-Raman studies requires further consideration. If single-sided exponential pulses are to be used for the γ pulse, to gain accurate lineshapes the spectral width should ideally be half that of the smallest homogeneous width of interest. It could be that if the gating effect of a single sided exponential pulse compromises spectral resolution too severely, a sequence such as Figure S7d might be the way forward. It is also worth noting a separate observation from the simulations. This is that the vibrational signal always peaks at $T_{\alpha\gamma} \sim 120$ fs when using a single sided exponential γ pulse.

The shape of the α pulse has also been discussed in 2D-IR studies.⁵ As it does not act in the same manner as the gating γ pulse, its effect on spectra is mainly one of spectral resolution and pathway / nonresonant background discrimination. Different spectral widths on the narrowed α pulse (reverse-single sided exponential, 2.5, 5, 10 and 20 cm^{-1}) were investigated in Experiment I (homodyne 2D-IR-Raman) and not found to have unusual effects on the data – other than lowering the resolution.

Section 4. Dispersed IR-Raman photon echo data.

In the main text, three kinds of plots of the dispersed IR-Raman photon echo signal were shown:

- i) A single $\omega_\beta - \omega_\alpha$ value and scanned $T_{\alpha\gamma}$ and $T_{\beta\gamma}$ (Figure 5),
- ii) Plots of the ‘echo cuts’ ($T_{\alpha\gamma} = 2T_{\beta\gamma}$) across the $\omega_\beta - \omega_\alpha$

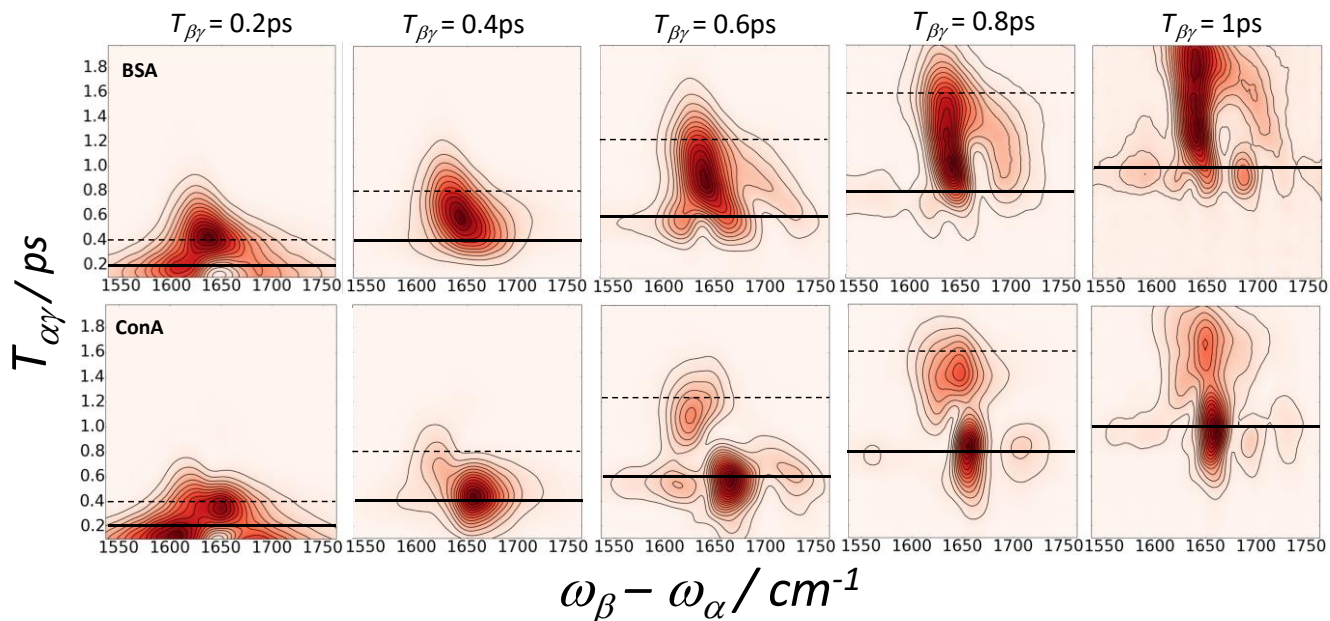


Figure S10. Amide I IR-Raman echoes from BSA (top row) and ConA (bottom row) viewed by plotting emission spectra as a function of $T_{\alpha\gamma}$ for fixed $T_{\beta\gamma}$. The dotted line is the spectrum of theoretical maximum rephasing time value, $T_{\alpha\gamma} = 2T_{\beta\gamma}$. The solid line marks the $T_{\alpha\gamma} = T_{\beta\gamma}$ point, at which all three diagrams contributing to the signal are selected (Figure 1, main text). For $T_{\alpha\gamma}$ delays later than this line, pathway 1 is selected.

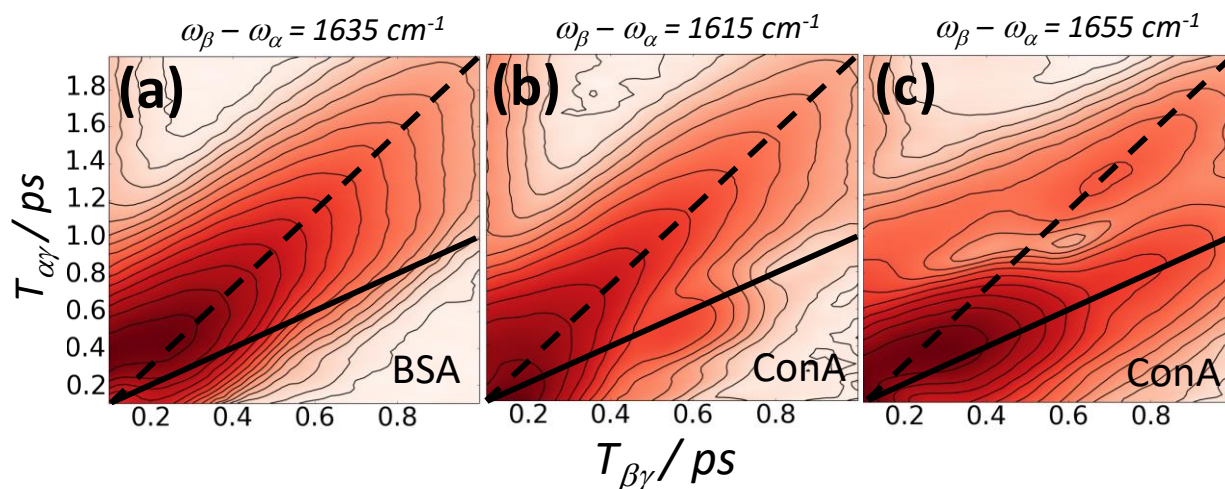


Figure S11. Logarithmic scale plots of IR-Raman signal for scanned $T_{\alpha\gamma}$ and $T_{\beta\gamma}$ at selected $\omega_{\beta} - \omega_{\alpha}$ values of the BSA and ConA data. The dotted line is the ‘echo cut’ line ($T_{\alpha\gamma} = 2T_{\beta\gamma}$). The solid line is where $T_{\alpha\gamma} = T_{\beta\gamma}$.

emission range (Figure 6).

iii) $T_{\beta\gamma}$ scans across the $\omega_{\beta} - \omega_{\alpha}$ emission range for fixed $T_{\alpha\gamma}$ (Figure 7).

Many alternative plots are possible, but were not shown in the main text for brevity. Figure S10 shows the ‘mirror’ of the main text Figure 7 plot, where $T_{\alpha\gamma}$ is scanned instead of $T_{\beta\gamma}$. The evolution of the signal is interesting for both the BSA and ConA. For the case of BSA, the echo appears to be earlier, but this is because scanning along the $T_{\alpha\gamma}$ coordinate includes more of the nonrephasing signals that peak

around $T_{\alpha\gamma} = T_{\beta\gamma}$ than when plotting scans along the $T_{\beta\gamma}$ coordinate. That this is so can be seen by inspecting the contours in the logarithmic plot Figure S11a.

The ConA data of Figure S11 is somewhat the opposite of the BSA data – it shows the echo across the entire amide I band more clearly than in the mirrored plot in the main text (Figure 7). The plots in Figure S11b and S11c show why the exponential fitting in the main text was successful at low emission frequencies (1615 cm^{-1}) and incorrect at higher frequencies (1655 cm^{-1}). In Figure S11c the signal oscillates along the rephasing line.

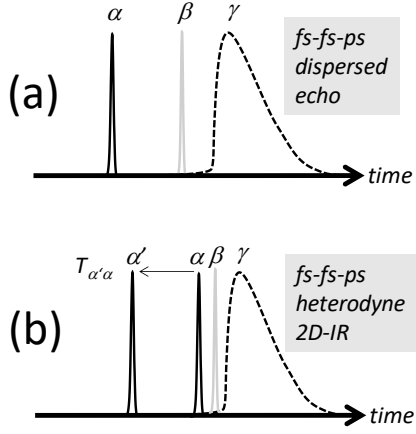


Figure S12. Dispersed echo and heterodyne detected FT-2D-IR-Raman pulse sequences.

Section 5. Calculation of heterodyne FT-2D-IR-Raman spectra.

Heterodyne 2D-IR-Raman experiments were performed in the main text using a pulse shaping scheme in a ‘homodyne-type’ geometry (Figure 3, main text and Figure S1b). It was shown how two replica α pulses generated via mid-IR acousto-optic pulse shaping could be used to recover a heterodyne detected 2D-IR-Raman spectrum *without* the need for a separate LO and any form of timing control post-LO generation. This route to heterodyne detection with mid-IR pulse shaping is different to those discussed previously.¹²

The heterodyne pulse sequence is shown in Figure 2d (main text). For clarity it is again reproduced here alongside the dispersed homodyne echo sequence in Figure S12. The two replica pulses, α and α' can be viewed as both making their own separate, collinear complex valued IR-Raman fields, each of which we consider to be of the form:

$$E_{\delta} = E_{NR} + E_R \quad \text{Eq.12}$$

i.e. the IR-Raman field E_{δ} comprises a nonresonant (NR) and a resonant (R) term. The α and α' pulses make individual fields E_{δ} and E'_{δ} . As is common in many other treatments of heterodyne detection, this shorthand for electric fields (denoted E) is not explicitly concerned with the temporal and spatial characteristics of the fields, but serves only to track of interference effects (cross terms). The pair of fields E_{δ} and E'_{δ} are collinear and interfere at each frequency point of the spectrometer focal plane, measured as a total intensity at each pixel of the CCD array:

$$I_{total} \propto |E_{\delta} + E'_{\delta}|^2 = E_{\delta}^2 + E'_{\delta}{}^2 + 2E_{\delta}E'_{\delta}\cos(\Delta\varphi) \quad \text{Eq.13}$$

The following steps and arguments describe how the required spectrum of the Het-FT-IR-Raman signal $E_R(\omega_{\alpha'})$ is extracted at each CCD pixel as a function of $\omega_{\alpha'}$. The quadratic (‘DC’) terms in Eq. 13 behave as a static background and the cross term of Eq. 13 is the quantity of interest. It is important to note that in this experimental approach, no delay between E_{δ} and E'_{δ} is introduced, as the visible γ pulse is common to both fields E_{δ} and E'_{δ} . It is their relative phase $\Delta\varphi$ which varies. Fixing the timing of the α and β pulses relative to γ to zero ($T_{\alpha\gamma} = T_{\beta\gamma} = 0$), if the timing of the replica pulse α' is scanned, the phase (and amplitude) of E'_{δ} relative to E_{δ} will oscillate (and diminish) over time. In other words, $E_{\delta}E'_{\delta}$ will oscillate with α' delay at the carrier frequency of ω_{α} over an envelope governed by the instrument response (nonresonant background) and by the vibrational free-induction decay of the sample.

Making the delay dependence explicit (denoting the $\alpha - \alpha'$ delay as $T_{\alpha\alpha'}$), we have for the Fourier Transform (FT) of the measured cross term intensity as a function of $T_{\alpha\alpha'}$:

$$FT[2E_{\delta}E'_{\delta}(T_{\alpha\alpha'})] \propto E_{\delta}E'_{\delta}(\omega_{\alpha'}) = E_{\delta}(E_{NR}(\omega_{\alpha'}) + E_R(\omega_{\alpha'})) \quad \text{Eq. 14}$$

Taking the real part of the Fourier Transform, we see that by using the E_{δ} signal as an ‘LO’, we are able to recover a spectrum of the nonresonant background and the IR-Raman signal in linear combination. The nonresonant spectrum $E_{NR}(\omega_{\alpha'})$ can be measured as a background simply by removing the IR-Raman ‘resonant’ component of the sample. Then we measure a heterodyne term of the form:

$$E_{\delta}^{bg} E_{NR}(\omega_{\alpha'}) \quad E_{\delta}^{bg} \neq E_{\delta} \quad \text{Eq. 15}$$

The fixed heterodyning field is now termed E_{δ}^{bg} , as it no longer contains any homodyne resonant IR-Raman signal. Neither E_{δ}^{bg} nor E_{δ} of Eq. 12 vary with $\omega_{\alpha'}$ but it is important to note that they are varying as a function of the detector axis frequency ω_{δ} . Taking the ratio of sample+background and background-only heterodyne measurements (Eq. 14 and 15), we have:

$$\frac{E_{\delta}(E_{NR}(\omega_{\alpha'}) + E_R(\omega_{\alpha'}))}{E_{\delta}^{bg} E_{NR}(\omega_{\alpha'})} = \frac{E_{\delta}}{E_{\delta}^{bg}} \left(1 + \frac{E_R(\omega_{\alpha'})}{E_{NR}(\omega_{\alpha'})} \right) \quad \text{Eq. 16}$$

$E_R(\omega_{\alpha'})$ is the quantity of importance. In understanding how Eq. 16 permits a measure of $E_R(\omega_{\alpha'})$, consider the following: $E_R(\omega_{\alpha'})$ is the amplitude spectrum of the IR-Raman signal. $E_{NR}(\omega_{\alpha'})$ is an amplitude spectrum of the nonresonant background which follows the amplitude

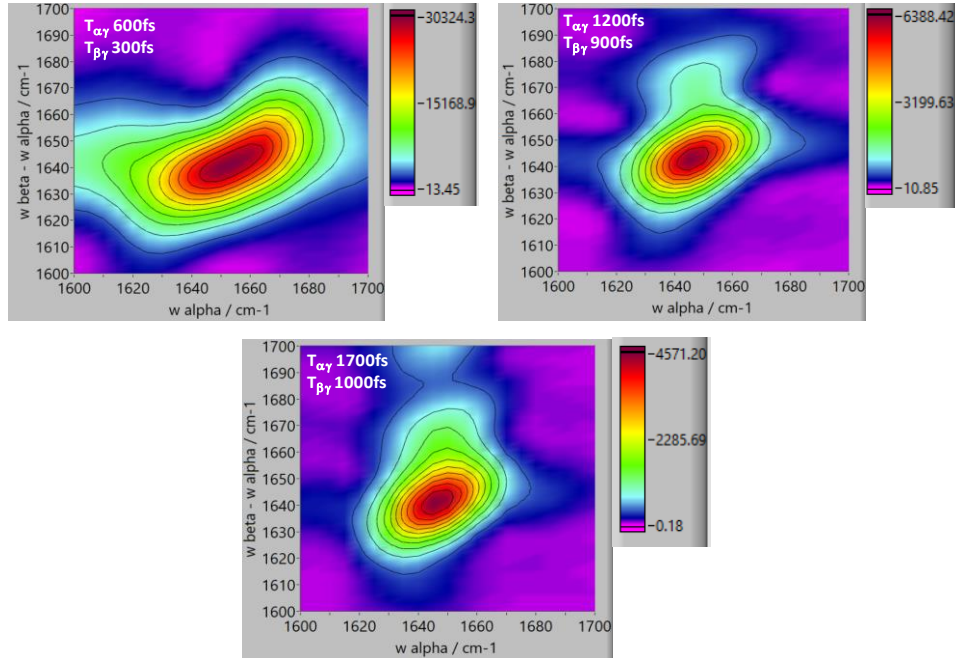


Figure S13. Solution phase homodyne IR-Raman 2D-IR-Raman spectra of ~ 50 mg / ml BSA in D_2O . 50 μm pathlength cell. The pulse shaper was set to 5 cm^{-1} spectral resolution (reverse etalon pulse shape). 2s averaging per frequency point and 5 cm^{-1} step size were used.

spectrum of the α pulse, and so in Eq. 16 it usefully normalises $E_R(\omega_{\alpha'})$. E_{δ} contains the nonresonant background and homodyne IR-Raman signal along the detection axis $\omega_{\beta} - \omega_{\alpha}$ (Eq. 12). Typically, $E_{NR} \gg E_R$. It follows that the ratio $E_{\delta}/E_{\delta}^{bg}$ in Eq. 16 is roughly constant, introducing only a minor perturbation to the spectrum across the detector axis which can be removed if necessary either by normalising across the detector axis from the parts of a processed spectrum where $E_{EVV}(\omega_{\alpha'}) = 0$ or by using the square root of the $T_{\alpha\alpha} = 0$ homodyne terms. Thus, heterodyne detection and time domain determination of the ω_{α} axis of the IR-Raman spectrum is possible in a homodyne geometry simply by using pulse shaping. This type of scheme ought also to be applicable to VSFG, with interesting potential advantages.

Section 6. Solution phase data

IR-Raman spectra of BSA solutions in D_2O in the range of 50 mg / ml BSA (equivalent to $\sim 0.5M$ residue concentration) in cells 50 μm pathlength using 1 mm thick CaF_2 window (front) and BK7 glass (back) are shown in Figure S13. These data are not dissimilar to the dried film spectra in the main text, demonstrating that solution phase amide I work is clearly viable.

Section 7. Coupled 2-level combination band Feynman and energy level diagrams

To aid the understanding of how the role of the IR and Raman pulses change between studying 3-level diagonal overtone states and coupled 2-level combination band cross

peaks in IR-Raman processes, the Feynman and wave mixing diagrams of pathways 1, 2 and 3 are shown in Figure S14 recast for coupled 2-level systems i and j .

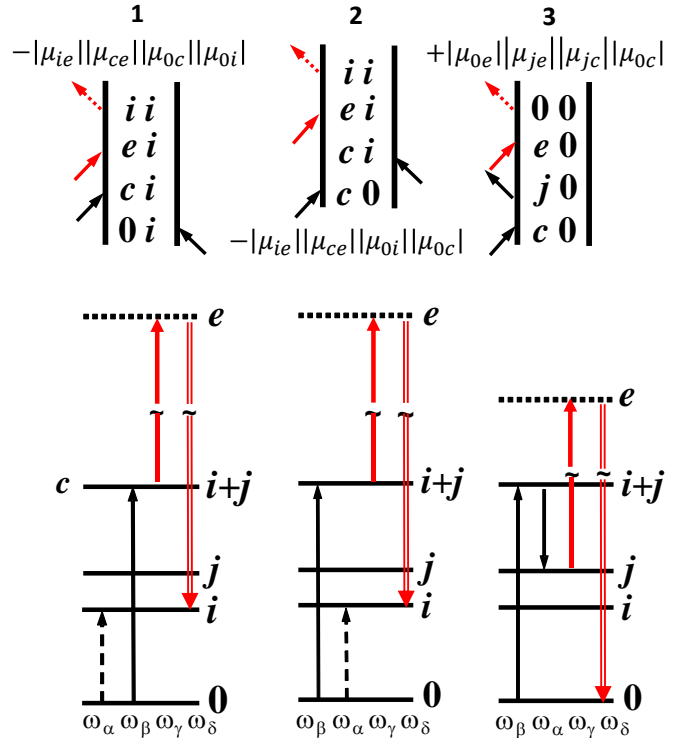


Figure S14. Feynman and energy level diagrams for IR-Raman processes for a combination band $c = i + j$. In terms of quantum numbers, $i=i'$ and $j=j'$.

64, pp 1311–1319.
<https://doi.org/10.1366/000370210793561673>.

ESI Bibliography

- (1) Zhao, W.; Wright, J. C. Doubly Vibrationally Enhanced Four Wave Mixing: The Optical Analog to 2D NMR. *Phys. Rev. Lett.* **2000**, *84* (7), 1411–1414.
<https://doi.org/10.1103/PhysRevLett.84.1411>.
- (2) Donaldson, P. M.; Greetham, G. M.; Shaw, D. J.; Parker, A. W.; Towrie, M. A 100 KHz Pulse Shaping 2D-IR Spectrometer Based on Dual Yb:KGW Amplifiers. *J. Phys. Chem. A* **2018**.
<https://doi.org/10.1021/acs.jpca.7b10259>.
- (3) Greetham, G. M.; Donaldson, P. M.; Nation, C.; Sazanovich, I. V.; Clark, I. P.; Shaw, D. J.; Parker, A. W.; Towrie, M. A 100 KHz Time-Resolved Multiple-Probe Femtosecond to Second Infrared Absorption Spectrometer. *Appl. Spectrosc.* **2016**, *70* (4), 645–653.
<https://doi.org/10.1177/0003702816631302>.
- (4) Marangoni, M.; Brida, D.; Cirmi, G.; Manzoni, C.; Cerullo, G.; Fusaro, D.; Pigozzi, F. M.; Capobianco, A. D.; Baronio, F.; Conforti, M.; et al. Tunable Narrow-Bandwidth Picosecond Pulses by Spectral Compression of Femtosecond Pulses in Second-Order Nonlinear Crystals. In *Optics InfoBase Conference Papers*; Optical Society of America, 2008.
<https://doi.org/10.1364/oe.15.008884>.
- (5) Shim, S. H.; Zanni, M. T. How to Turn Your Pump-Probe Instrument into a Multidimensional Spectrometer: 2D IR and Vis Spectroscopies via Pulse Shaping. *Physical Chemistry Chemical Physics*. The Royal Society of Chemistry February 7, 2009, pp 748–761.
<https://doi.org/10.1039/b813817f>.
- (6) Clark, I. P.; Towrie, M. A Compact Micro-Bolometer Array for Mid-Infrared Laser Beam Alignment, Diagnostics and Spot-Size Measurement. *Pre Print* **2019**.
<https://doi.org/10.20944/preprints201912.0085.v1>.
- (7) Shim, S. H.; Strasfeld, D. B.; Ling, Y. L.; Zanni, M. T. Automated 2D IR Spectroscopy Using Mid-IR Pulse Shaping and Applications to Membrane Peptides. In *Optics InfoBase Conference Papers*; 2007. <https://doi.org/10.1364/ls.2007.lwg2>.
- (8) Greetham, G. M.; Burgos, P.; Qian, C.; Clark, I. P.; Codd, P. S.; Farrow, R. C.; George, M. W.; Kogimtzis, M.; Matousek, P.; Parker, A. W.; et al. ULTRA: A Unique Instrument for Time-Resolved Spectroscopy. In *Applied Spectroscopy*; 2010; Vol. 64, pp 1311–1319.
<https://doi.org/10.1366/000370210793561673>.
- (9) Hamm, P.; Zanni, M. *Concepts and Methods of 2D Infrared Spectroscopy*; Cambridge University Press, 2011; Vol. 9781107000056.
<https://doi.org/10.1017/CBO9780511675935>.
- (10) Cho, M. Theoretical Description of the Vibrational Echo Spectroscopy by Time-Resolved Infrared-Infrared-Visible Difference-Frequency Generation. *J. Chem. Phys.* **1999**, *111* (23), 10587–10594.
<https://doi.org/10.1063/1.480411>.
- (11) Meyer, K. A.; Wright, J. C. Interference, Dephasing, and Coherent Control in Time-Resolved Frequency Domain Two-Dimensional Vibrational Spectra. *J. Phys. Chem. A* **2003**, *107* (41), 8388–8395.
<https://doi.org/10.1021/jp035146+>.
- (12) Laaser, J. E.; Xiong, W.; Zanni, M. T. Time-Domain SFG Spectroscopy Using Mid-IR Pulse Shaping: Practical and Intrinsic Advantages. *J. Phys. Chem. B* **2011**, *115* (11), 2536–2546.
<https://doi.org/10.1021/jp200757x>.